

Sliding Wear Behavior of Spark Plasma-Sintered Cu–6 Wt Pct Cr Alloy at Room and Elevated Temperatures



SHUAI PAN, CANCAN ZHAO, WEIWEI ZHU, FEILONG JIANG, JIAN ZHOU,
and FUZENG REN

Although dilute Cu-Cr alloys are frequently used for applications involving sliding contacts, their wear mechanism at elevated temperatures has rarely been explored. We fabricated a bulk Cu-6 wt pct Cr alloy using high-energy ball milling and spark plasma sintering, and systematically investigated its dry sliding wear behavior against 440C stainless steel at room temperature and 300 °C. The alloy had a heterogeneous microstructure consisting of coarse-grained Cu (average grain size: 1.5 μm) distributed into a nanocrystalline Cu-Cr matrix (average Cu grain size: 77 nm; Cr-rich precipitate size: 18 nm), which gave high strength and plasticity (ultimate compressive strength: 1020 MPa; strain-to-failure: 26.0 pct) at room temperature. At 300 °C, the strength was significantly reduced, the coefficient of friction and wear rate increased, and the dominant wear mode switched from adhesive wear to oxidative/abrasive wear. Uniformly distributed nanoscale Cr-rich and Cr oxide precipitates hindered severe plastic deformation near the sliding surface during wear at room temperature; at 300 °C, severe plastic deformation was observed, with elongated Cu grains and uniformly dispersed Cr-rich and Cr oxide nanoparticles. Formation of a discontinuous glaze layer consisting of equiaxed nanograins of Cu, Cu oxides, and Cr oxides resulted in severe abrasion-assisted wear, and reduced the wear resistance at 300 °C.

<https://doi.org/10.1007/s11661-019-05243-8>

© The Minerals, Metals & Materials Society and ASM International 2019

I. INTRODUCTION

COPPER-CHROMIUM (Cu-Cr)-based alloys are widely used for trolley wires in electric railways, spot welding electrodes, casting molds, and tubes of crystal-lizers,^[1–9] due to their combination of adequate strength, high fatigue resistance, high thermal and electrical conductivity and excellent wear resistance at high-operating pressures and moderate temperatures (250 °C to 450 °C).

Precipitation hardening by aging treatments is a common approach to increase strength and hardness of Cu-Cr-based alloys.^[1,6,9,10] Microstructure,^[11–13] mechanical properties,^[2,3,14,15] and aging kinetics^[16] of these alloys have been systematically explored, with particular focus on morphology, composition, crystallography, and distribution of the precipitates in a coarse-grained Cu matrix and their correlation with mechanical and physical properties. Precipitation strengthening by conventional processes is limited owing to the low solubility of Cr in a Cu matrix,^[14] so considerable efforts have been devoted to enhancing the mechanical properties through microstructure refinement. Various severe plastic deformation (SPD) techniques, including accumulative roll-bonding (ARB),^[3] high-pressure torsion (HPT),^[6,17–19] and equal channel angle pressing (ECAP),^[20–23] have been used to produce bulk ultrafine-grained (UFG) or nano-grained Cu-Cr alloys.^[24] With a combination of precipitation strengthening and grain boundary strengthening, the fabricated Cu-Cr alloys show significantly higher strength than their coarse-grained counterparts.^[20–23] Bulk UFG or nanostructured alloys processed by SPD, however, often have a size (especially thickness) limitation.

SHUAI PAN and FEILONG JIANG are with the Department of Materials Science and Engineering, Southern University of Science and Technology, Shenzhen, P.R. China and also with the School of Materials Science and Engineering, Harbin Institute of Technology, Harbin, P.R. China. CANCAN ZHAO and FUZENG REN are with the Department of Materials Science and Engineering, Southern University of Science and Technology. Contact e-mail: renfz@sustech.edu.cn WEIWEI ZHU is with the Department of Materials Science and Engineering, Southern University of Science and Technology and also with the Institute of Applied Physics and Materials Engineering, Faculty of Science and Technology, University of Macau, Macau, P.R. China. JIAN ZHOU is with the Shagang School of Iron and Steel, Soochow University, Suzhou, P.R. China.

Manuscript submitted November 8, 2018.

Article published online May 7, 2019

Mechanical alloying by high-energy ball milling (HEBM) can produce nanostructured powders in immiscible alloys,^[25–27] but grains are coarsened during the subsequent compaction into bulk at high temperature by conventional sintering.^[28] Lower sintering temperatures and shorter sintering times of spark plasma sintering (SPS) could suppress grain growth during sintering and preserve the nanocrystalline microstructure formed by HEBM.^[29,30] Combining HEBM and SPS provides a simple and effective processing procedure to produce bulk UFG or even nanostructured alloys with relatively large size.

Apart from strength, the sliding wear performance, particularly at elevated temperatures, is critical to determine the lifetimes of Cu-Cr-based alloys for a wide range of applications and has attracted much research interest. Purcek *et al.*^[1,6] showed that the precipitates dispersed within a UFG matrix significantly increased the wear resistance of a Cu-Cr-Zr alloy. Kouhanjani *et al.*^[31,32] showed that an intermetallic wear-induced layer was created during wear of cold-worked Cu-0.65 wt pct Cr alloy. Qi *et al.*^[33] showed that the formation of fine, dispersed, and coherent precipitates in the Cu matrix could improve the hardness and wear resistance of a Cu-Cr-Zr alloy, and revealed the wear mechanisms under unlubricated conditions. Most investigations have, however, focused on the friction and wear behavior of Cu-Cr-based alloys at room temperature (RT), where the wear resistance mainly depends on the material's hardness and sliding-induced microstructure evolution below the sliding surface.^[34–36] At elevated temperatures, the surfaces of the alloys are not only subjected to the mechanical stress, but are also susceptible to thermal softening, grain growth and oxidation by reaction with oxygen, which may significantly change their overall wear performance.^[34] Tribochemical reactions during wear may result in the formation of a 'glaze layer', which is mainly composed of compacted wear debris or metallic oxides and leads to a transition from severe wear to mild wear.^[37–42]

Cu-Cr alloys are often operated at moderate temperatures in the range of 250 °C to 450 °C, but their wear and deformation mechanisms in this temperature range have rarely been reported. This motivated us to explore the sliding wear behavior of these alloys at moderate temperatures, which is essential to understanding their wear performance in a service environment. A bulk Cu-6 wt pct Cr alloy with heterogeneous microstructure was fabricated using a combination of HEBM and SPS. Based on detailed characterization of the microstructure of the sintered alloy and examination of its mechanical properties, its dry sliding wear behavior was systematically investigated at both RT and 300 °C, with particular focus on the sliding wear-induced microstructural evolution and wear mechanisms at moderate temperature.

II. EXPERIMENTAL

A. Fabrication of Cu-6 Wt Pct Cr Alloy

Commercially pure copper (Alfa Aesar, 10 μm , 99.9 pct) and chromium (Alfa Aesar, < 10 μm , 99.2 pct) powders with nominal composition of Cu-6 wt pct Cr were used as the starting material. The powder mixture and hardened steel balls were loaded into a hardened steel vial at a mass ratio of 1:5 and subjected to HEBM using a SPEX 8000D mill (SPEX SamplePrep, USA) at RT [(25 \pm 1) °C] in an argon glove box for 20 hours. Stearic acid (1 wt pct) was added as a process control agent to prevent the powder from cold welding. The ball-milled powder was dried at 110 °C in a vacuum oven to vaporize the stearic acid. To investigate forced chemical mixing of the Cu-6 wt pct Cr system, both the starting powder mixture and the powders after ball milling for varying times were analyzed by X-ray diffraction (XRD).

The 20-h-ball-milled powder was packed into a graphite die with an inner diameter of 10 mm and then compacted by SPS (SPS-211Lx, Fujidempa Kogyo Co., Ltd., Japan) at 750 °C and 50 MPa for 10 minutes in a vacuum. The consolidated bulk samples were ground with SiC emery papers and then vibrationally polished (VibroMet™ 2, Buehler, USA) with diamond and alumina suspensions. The density of the as-sintered samples, as measured by the Archimedes method (ASTM B962-15), exceeded 98 pct.

B. Mechanical and Wear Testing

Micro-hardness of the sintered alloy was measured using a high-temperature Vickers diamond pyramidal indenter (Archimedes Industrial Technology Co., Ltd., London, United Kingdom) under a load of 3 kgf for 5 seconds. At least five individual measurements were performed; the average values with standard deviations are reported. Nano-hardness was measured at RT using a Hysitron TI-950 Triboindenter with a diamond Berkovich tip and calibrated with standard aluminum and fused quartz. At least ten indentations were performed for each sample and the average values are reported. Following the Chinese GB/T 7314-2005 standard, uniaxial compression tests were performed at RT and 300 °C with an initial quasi-static strain rate of $5.0 \times 10^{-3} \text{ s}^{-1}$, using a universal testing machine (DDL100, Sinotest Equipment Co., Ltd., China).

Prior to the wear tests, pins of 3 mm in diameter and 6 mm in length were cut from the bulk cylindrical samples using electrical discharge machining. Both the surfaces of the pins and the counter-body disk were mechanically polished with SiC papers down to 1200 grit. Considering that Cu-Cr alloys have been widely used for tubes of crystallizers, we selected martensitic 440C stainless steel (SS 440C) with a hardness of \sim 300

HV as the mating material. Pin-on-disk wear tests (Pin-on-Disk Tribometer, Anton-Parr, Austria) were performed in air at RT and 300 °C under a load of 5 N at a constant sliding velocity of 0.1 m/s with a total sliding distance up to 1000 m. Wear rates were calculated according to the following equation:

$$w = \frac{M_{\text{loss}}}{P \times L \times \rho}, \quad [1]$$

where M_{loss} is the weight loss of the pins, P is the applied load, L is the sliding distance and ρ is the density of the pins. Before weighing, the pins were ultrasonically cleaned with 100 pct acetone for 10 minutes. Three independent tests were run at each temperature and average wear rates and coefficient of friction values were determined.

C. Microstructural Characterization

The phases of the powders and bulk samples were identified by XRD recorded by a diffractometer in the 2θ range from 10 to 100 deg using Cu-K α radiation (Smartlab-9 kW, Rigaku, Japan; $\lambda = 0.154056$ nm, 45 kV, 200 mA) with a step size of 0.02 deg and speed of 10 deg/minute.

Morphology and chromium distribution of the sintered bulk sample were characterized by scanning electron microscopy (SEM; TESCAN MIRA 3, Czech Republic) equipped with an energy-dispersive X-ray spectroscopy (EDX; AZtec EDX system with an X-Max^N 50 mm² silicon drift detector, Oxford Instruments, UK). Surface morphology of the worn pins and disks was analyzed by SEM. The SS 440C disk also contained 16-18 wt pct Cr, so Cu and Fe were traced to distinguish the pin and disk materials. Surface profiles were measured using a three-dimensional (3D) optical microscope (ContourGT-K, Bruker, Germany). Phases, morphologies, and chemical compositions of wear debris were characterized by XRD, SEM, and EDX, respectively. Microstructures of the bulk samples before and after wear were characterized by secondary-electron (SE) imaging of a focused ion beam (FIB; Helios NanoLabTM 600i, FEI, USA) on milled cross-sections, transmission electron microscopy (TEM), high-resolution TEM (HRTEM), and high-angle annular dark-field scanning TEM (HAADF-STEM; Tecnai G2 TF30 S-Twin, FEI, USA) with an attached EDX, operated at 300 kV. All TEM samples were prepared by FIB milling using a site-specific standard lift-out technique. The directions normal to the sliding surface, along the sliding direction and perpendicular to the sliding direction in the sliding plane were defined as ND, SD, and TD, respectively. ND-SD cross-sectional TEM samples were prepared. To protect the original worn surface, a platinum (Pt) cap layer with thickness of $\sim 1 \mu\text{m}$ was deposited using an ion beam before milling the trench. To minimize surface damage by Ga⁺ ion implantation, the acceleration voltage was reduced to 2 kV during the final step of polishing. Grain/precipitate size distributions in both the matrix and precipitates were statistically measured from HAADF-STEM images. The

images were analyzed using the Heyn (4) Lineal Intercept Procedure in accordance with ASTM E112-10 (Standard Test Methods for Determining Average Grain Size). At least 100 grains/precipitates were measured to determine the mean lineal intercept length.

III. RESULTS

A. Phase and Microstructure of As-Sintered Cu-6 Wt Pct Cr Alloy

Phase evolution of the powders during ball milling and subsequent SPS was characterized. The XRD pattern (Figure 1(a)) of the starting Cu-6 wt pct Cr powder clearly showed the Cr (110) diffraction peak at $2\theta \sim 44.4$ deg. With an increase of ball milling time, the intensities of both the Cu and Cr reflections were significantly reduced and the diffraction peaks were broadened (Figures 1(b, c)), due to grain refinement and lattice strain. The XRD patterns showed almost no difference between the powder after ball milling for 18 and 20 hours, which meant that the system had reached a relatively stable state; therefore, we used 20 hours-ball-milled powder for the subsequent SPS.

In comparison with the XRD pattern of the starting powder, after 20 hours of ball milling, the Cu (111) reflection at $2\theta = 43.32$ deg slightly shifted (0.15 deg) to a larger 2θ angle and the Cr (110) reflection at $2\theta \sim 44.4$ deg was still visible, albeit with very weak intensity, suggesting formation of a Cu-Cr supersaturated solid solution and existence of some remaining body-centered cubic (bcc) Cr phase.^[5] The formation of Cu-Cr supersaturated solid solution was caused by forced chemical mixing induced by SPD during HEBM, which is known to increase the solubility in many immiscible alloy systems.^[25,43-45] The presence of remaining bcc Cr phase was due to the large positive heat of mixing of Cu-Cr (12 kJ/mol)^[46] and, thus, only very limited intermixing was observed, as frequently found in other face-centered cubic (fcc)-bcc systems.^[47]

An XRD pattern of the spark plasma-sintered bulk Cu-6 wt pct Cr alloy is shown in Figure 1(b). All peaks became sharp again, indicating grain growth and strain release during SPS. In addition to the Cu and bcc Cr phases, a trace amount of Cr oxide was also detected.

Detailed microstructural characterization of the spark plasma-sintered Cu-6 wt pct Cr alloy was undertaken. Figure 2(a) shows a backscattered secondary-electron (BSE) image of the alloy. In addition to several pores, shown as black contrast, the alloy exhibited two distinct contrasts. EDX elemental maps revealed that the matrix (gray contrast) showed a uniform distribution of Cu and Cr, while the other region (relatively bright contrast) only contained Cu: no Cr was detected. High-magnification SE images (Figures 2(c, d)) of FIB-milled cross-sections revealed that the Cu zone had a coarse-grained microstructure with an average grain size of $\sim 1.5 \mu\text{m}$, while the matrix had a nanocrystalline microstructure. HAADF-STEM and TEM characterizations of this latter region revealed further detail of its microstructure. HAADF-STEM (Figure 3(a)) and EDX

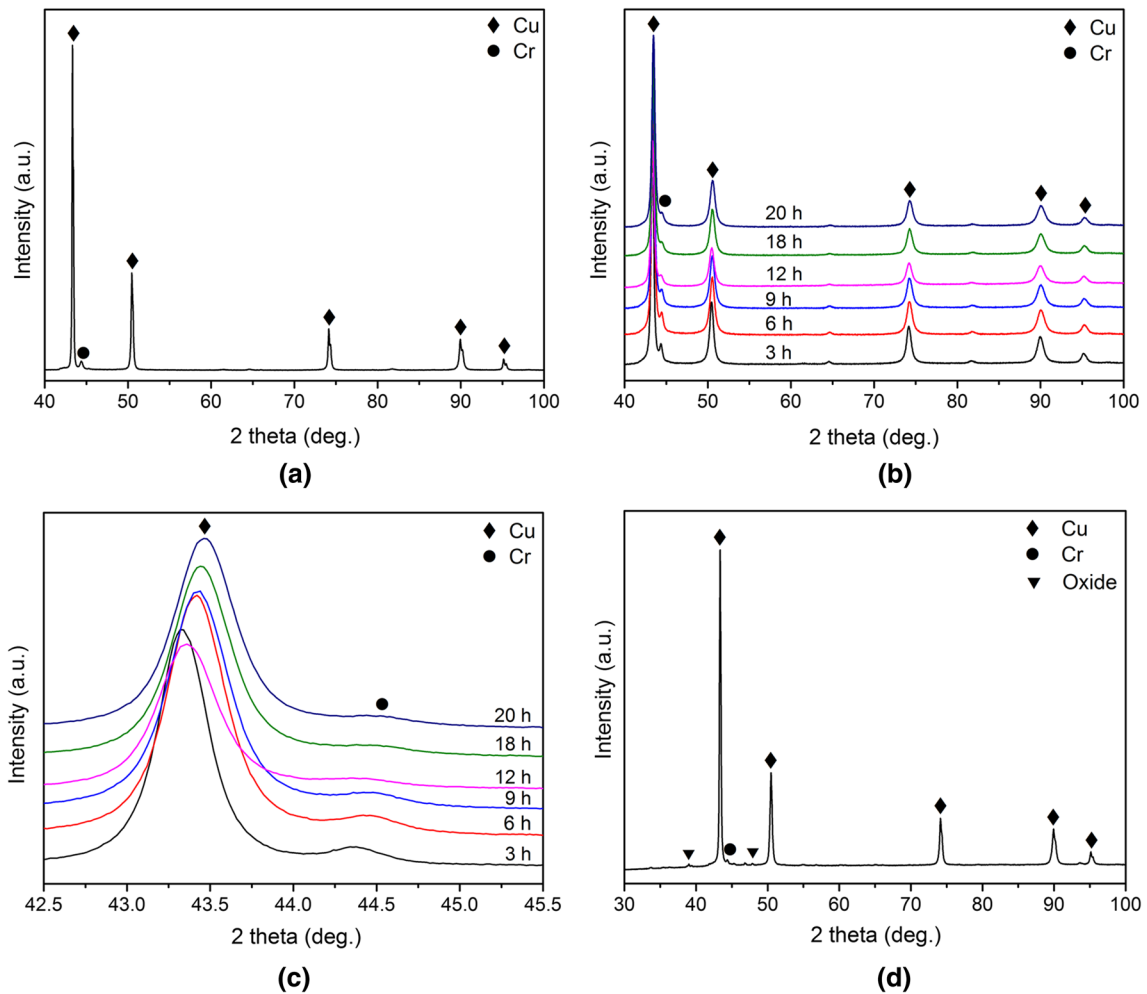


Fig. 1—XRD patterns of Cu-6 wt pct Cr powder and consolidated alloy. (a) Starting Cu and 6 wt pct Cr powder; (b) powders after ball milling for different times; (c) enlarged XRD patterns with 2θ in the range of 42.5 to 45.5 deg; (d) consolidated Cu-6 wt pct Cr alloy.

(Figure 3(b)) analyses showed that the nanocrystalline matrix consisted of three phases: (1) the bright contrast corresponded to Cu; (2) the gray area was Cr-rich nano-precipitates; and (3) the dark area was Cr oxides. Statistical measurements from the HAADF-STEM images (Figure 4) showed that the average sizes of the Cu grains and Cr-rich precipitates (averaged over more than 100 grains/precipitates) were 77 and 18 nm, respectively. Both their sizes followed a normal distribution (Figures 4(b, c)). A bright-field TEM image and corresponding selected-area electron diffraction (SAED) pattern are presented in Figure 3(c). Only Cu and bcc Cr were present in the SAED pattern, while no Cr oxide was detected. This further confirmed that the amount of Cr oxide was rather limited, consistent with the XRD pattern shown in Figure 1(b). The inter-planar distance (d) calculated from the SAED pattern for Cu (111) was slightly larger (about 0.002 nm) than that of pure Cu (JCPDS No. 70-3038), suggesting that supersaturated solid solution still existed in the Cu-Cr alloy.

This detailed microstructural characterization demonstrated that this Cu-6 wt pct Cr alloy, fabricated using a combination of HEBM and SPS, contained a heterogeneous microstructure of nanocrystalline Cu-Cr matrix and coarse-grained Cu.

B. Mechanical Properties of Spark Plasma-Sintered Cu-6 Wt Pct Cr Alloy

Mechanical properties of the fabricated Cu-6 wt pct Cr alloy were measured. Micro-hardness values of this alloy at RT and 300 °C were measured to be 246 (± 5) and 185 (± 2) HV, respectively. Compared with other dilute Cu-Cr alloys fabricated by SPD,^[48–50] the present Cu-6 wt pct Cr alloy showed the highest micro-hardness value at RT. To further distinguish the hardness difference between the coarse-grained Cu and nanocrystalline Cu-Cr matrix, nano-hardness tests were performed at RT in these two regions, as shown in Figure 5. The average value of the nano-hardness of

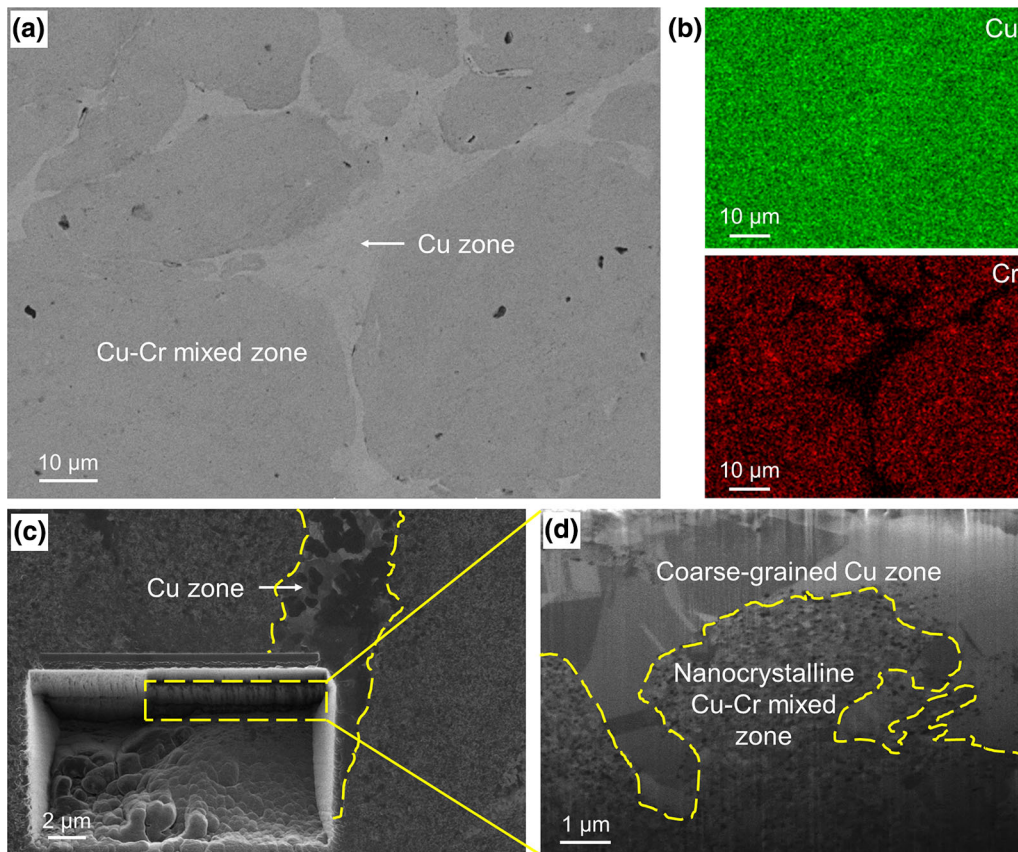


Fig. 2—Microstructure of spark plasma-sintered Cu-6 wt pct Cr alloy. (a) BSE image; (b) EDX elemental map showing the distributions of Cu and Cr in (a); (c) SE image of a representative site for FIB milling; (d) SE image of an FIB-milled cross-section.

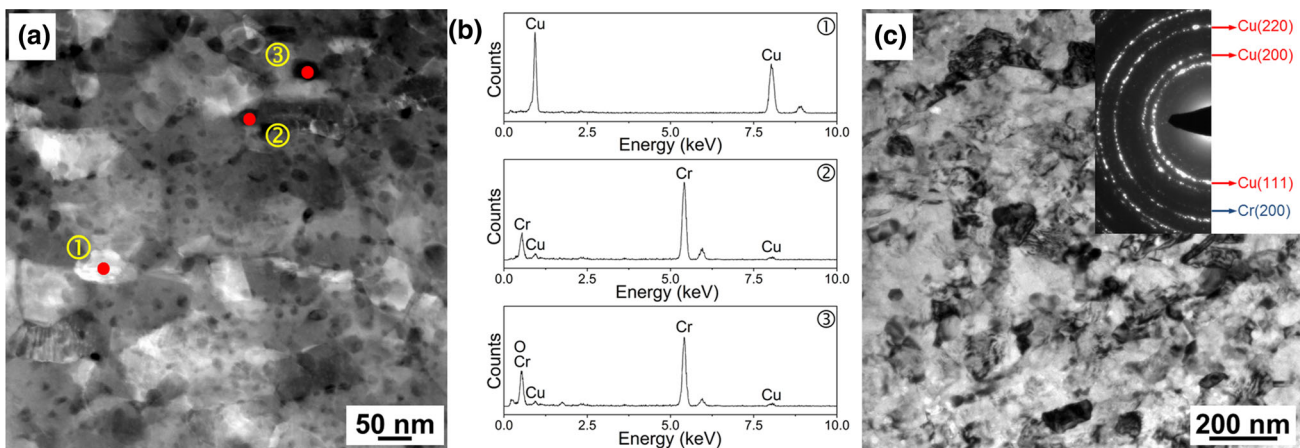


Fig. 3—STEM/TEM characterization of nanocrystalline Cu-Cr matrix. (a) HAADF-STEM image; (b) EDX spectra obtained from the three contrasts in (a); (c) bright-field TEM image with corresponding SAED pattern.

coarse-grained Cu and nanocrystalline Cu-Cr matrix were $1.38 (\pm 0.25)$ GPa and $2.74 (\pm 0.23)$ GPa, respectively. The compressive stress-strain curves at RT and $300\text{ }^{\circ}\text{C}$ are presented in Figure 6. The yield strength,

ultimate compressive strength, and strain-to-failure at RT reached 709, 1020 MPa and 26.0 pct, respectively. This combination of high strength and good plasticity was attributed to the heterogeneous microstructure of

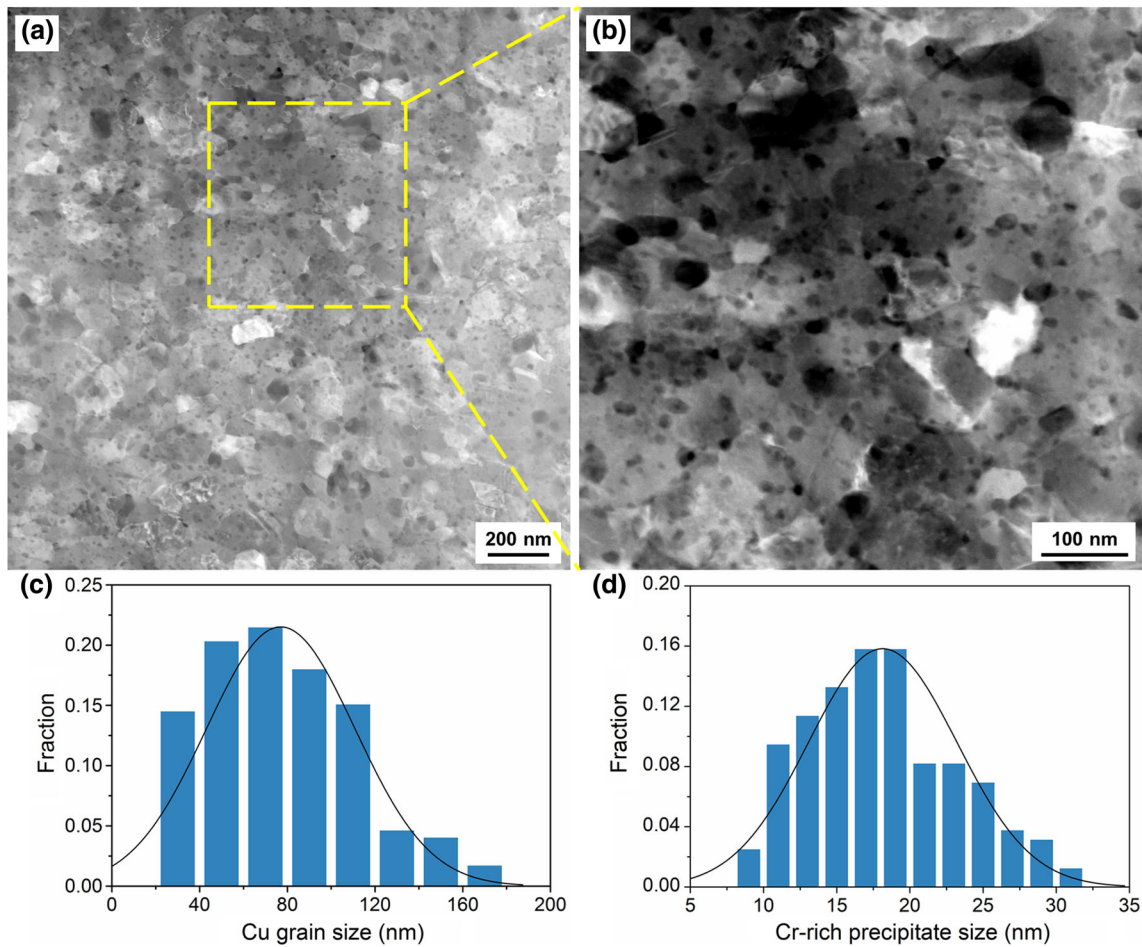


Fig. 4—Cu grain and Cr-rich precipitate size distributions of nanocrystalline Cu-Cr matrix in the spark plasma-sintered Cu-6 wt pct Cr alloy. (a) and (b) show HAADF-STEM images at different magnifications; (c) and (d) show Cu grain size and Cr-rich precipitate size distributions, respectively.

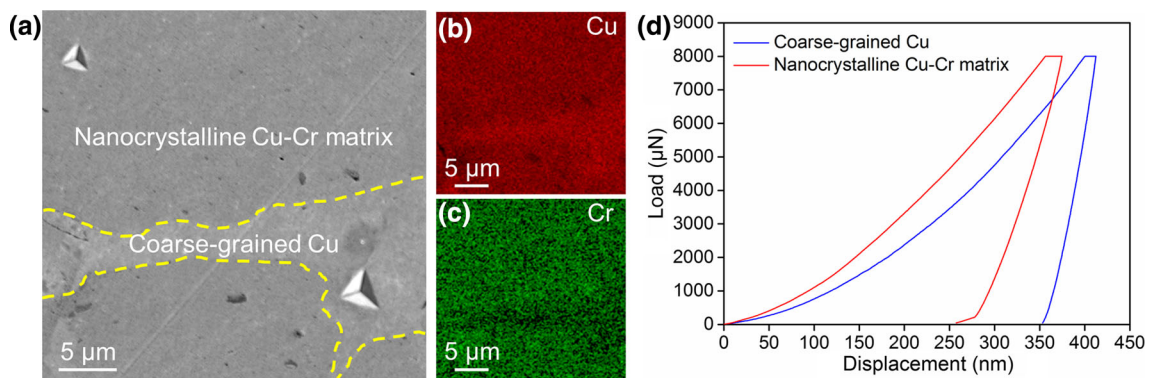


Fig. 5—Nano-hardness tests of the spark plasma-sintered Cu-6 wt pct Cr alloy. (a) Representative SEM image with indents at nanocrystalline Cu-Cr matrix and coarse-grained Cu; (b) and (c) EDX elemental maps of (a); (d) nanoindentation load-displacement curves with a maximum load of 8000 μN .

the alloy, in which the nanocrystalline matrix and uniform dispersion of Cr-rich nano-precipitates contributed to the high strength, while the coarse-grained Cu contributed to the plasticity. At 300 °C, the yield

strength and ultimate compressive strength decreased to 287 and 322 MPa, respectively, while no fracture was observed for the Cu-Cr alloy during the compressive tests.

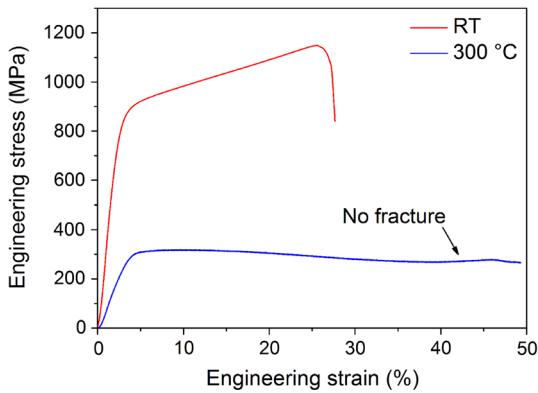


Fig. 6—Compressive stress–strain curve of spark plasma-sintered Cu-6 wt pct Cr alloy at RT and 300 °C.

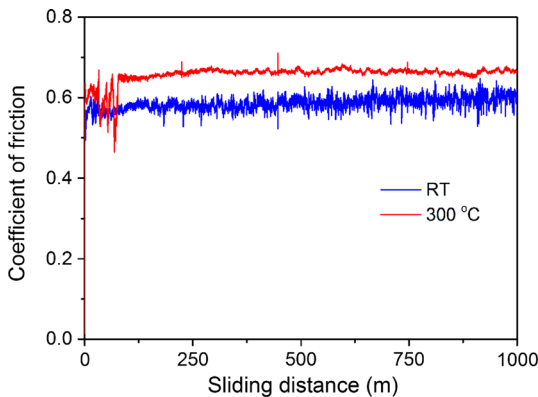


Fig. 7—Coefficient of friction as a function of sliding distance at RT and 300 °C for Cu-6 wt pct Cr alloy sliding against a SS 440C disk under a load of 5 N and at a sliding velocity of 0.1 m/s.

C. Coefficient of Friction and Wear Rates

Coefficient of friction of the bulk Cu-6 wt pct Cr alloy as a function of sliding distance at RT and 300 °C is plotted in Figure 7. At both temperatures, the tribo-system reached steady-state wear over a sliding distance of about 100 m. The steady-state coefficient of friction of wear at 300 °C (0.67 ± 0.01) was slightly higher than that at RT (0.62 ± 0.03). The measured wear rate of the alloy at 300 °C was $5.73 (\pm 0.59) \times 10^{-4} \text{ mm}^3/(\text{N m})$, which was more than twice that at RT ($2.50 (\pm 0.17) \times 10^{-4} \text{ mm}^3/(\text{N m})$). The coefficient of friction and wear rate of this Cu-6 wt pct Cr alloy at RT were close to those reported for a Cu-10 at. pct W alloy fabricated by HEBM and warm pressing.^[51]

D. Morphology, Size and Composition of Wear Debris

The morphologies and chemical compositions of the wear debris collected after wear testing are presented in Figure 8. At RT, the debris consisted of large flakes with an average size of about 150 μm , similar to that frequently observed in other Cu-based alloys after sliding wear tests.^[1,4,52,53] The EDX spectrum in Figure 8(b) showed that the debris contained Cu, Cr, Fe, and O; the XRD pattern (Figure 8(c)) showed that

the debris mainly comprised Cu with a minor amount of Cr_2O_3 . In contrast, the size of the wear debris generated from wear at 300 °C ranged from several microns to $\sim 150 \mu\text{m}$ (Figure 8(d)) in size and much more oxygen was detected, as evidenced by the strong oxygen peak in Figure 8(e). The XRD pattern in Figure 8(f) further revealed that besides Cu, large amounts of Cu oxides and Cr oxide were observed, including CuO, Cu_2O and Cr_5O_{12} . The composition and phase analyses revealed that, at both RT and 300 °C, the generated wear debris mainly originated from the pin material, especially at 300 °C.

E. Surface Morphology, Composition and Profile of Worn Pins

Figure 9 presents a comparison of typical surface morphology, composition, and profiles of the worn pins at RT and 300 °C. At RT, the worn pin showed features of localized material flow and extrusion (Figure 9(a)), which are typical characteristics of adhesive wear. EDX elemental maps (Figure 9(b)) showed that the surface composition consisted of dominantly Cu and Cr with uniform distributions, and a rather low concentration of Fe and O in some regions, which suggested that a trace amount of counterface material was transferred onto the pin surface. The correlated distribution of Fe and O indicated the formation of iron oxides during wear. Figure 9(c) shows the 3D surface profile over an area of $850 \mu\text{m} \times 1130 \mu\text{m}$. Scattered peaks were observed on the worn surface with roughness (R_a) of 1.777 μm .

At 300 °C, the worn pin surface showed a distinct appearance from that at RT, in the form of parallel grooves, which was proof of abrasive wear (Figure 9(d)). EDX elemental maps (Figure 9(e)) showed that, besides the uniformly distributed Cu and Cr, much higher concentrations of Fe and O were detected (Figure 9(f)). Except for fresh surface exposed within grooves, as denoted in a representative region in Figure 9(d), the surface was mostly covered by oxides. A 3D profile (Figure 9(f)) also clearly showed such parallel grooves/ridges with lower roughness of $R_a = 0.743 \mu\text{m}$.

F. Surface Morphology, Composition and Profile of Wear Tracks

Figure 10 presents a comparison of typical surface morphology, composition, and profile of the wear tracks at RT and 300 °C. At RT, the SEM image (Figure 10(a)) and the EDX elemental maps (Figure 10(b)) showed that more than half of the surface was covered by strong shear-deformed Cu patches transferred from the pin and that the O signals were very weak. The 3D profile in Figure 10(c) showed that most areas of the disk surface after wear were at a similar height and some pits were irregularly distributed. In contrast, at 300 °C, the disk surface was covered by fine oxides, but there was still evidence of grooves (Figure 10(d)). EDX elemental maps (Figure 10(e)) demonstrated that almost the entire surface was covered by Cu transferred from the pin material and a significantly higher concentration of O was

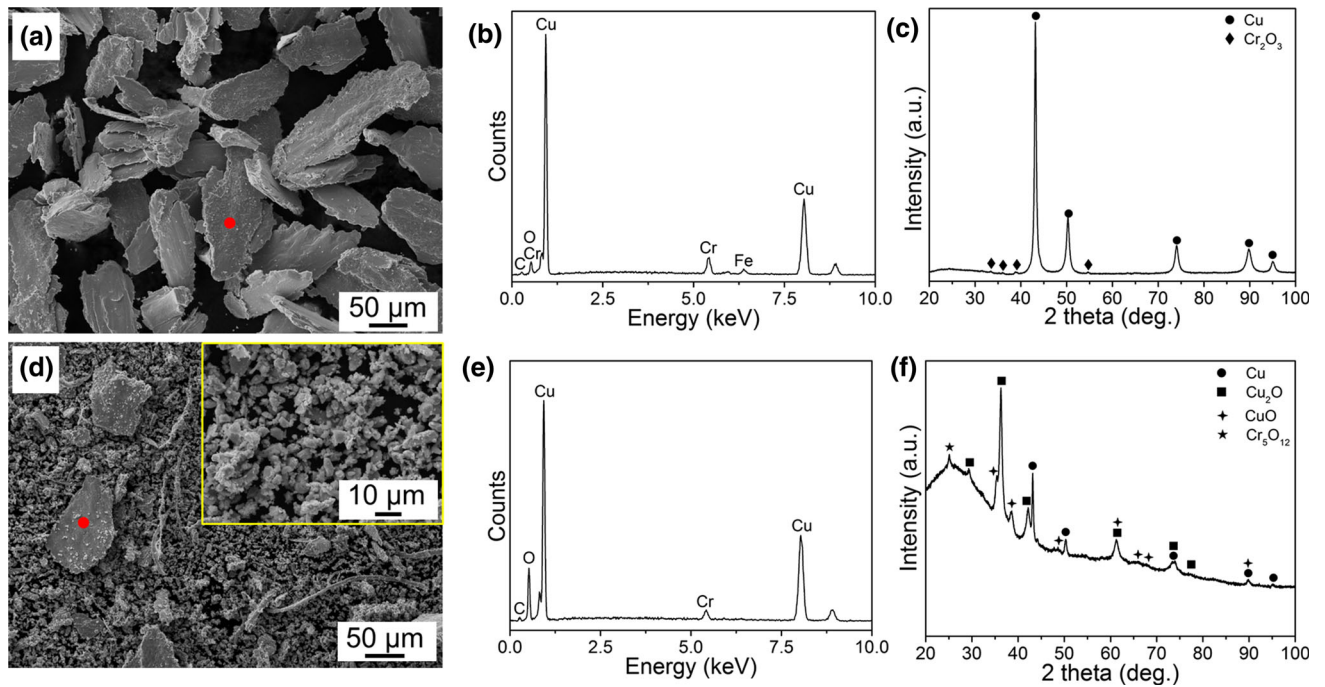


Fig. 8—Characterization of the wear debris of Cu-6 wt pct alloy sliding against SS 440C at room temperature and 300 °C. (a) through (c) show an SEM image, EDX spectrum, and XRD pattern of the wear debris generated at room temperature, respectively; (d) through (f) show the analogous data generated at 300 °C.

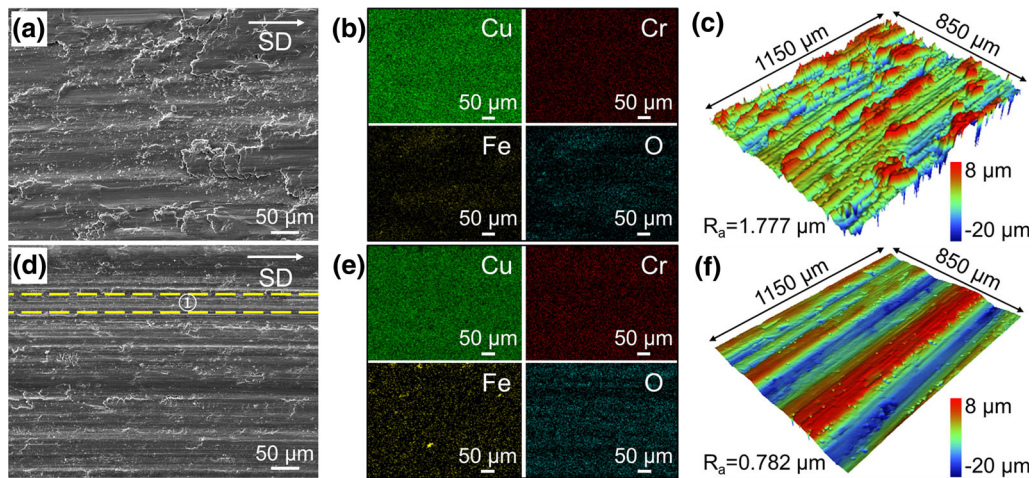


Fig. 9—Characterization of worn pin surfaces upon wear exposure at room temperature and 300 °C. (a) through (c) show an SEM image, EDX elemental maps, and 3D surface profile of the worn pin measured at RT, respectively; (d) through (f) show the analogous data measured at 300 °C.

detected. The O was uniformly distributed on the disk surface. The 3D surface profile (Figure 10(f)) clearly revealed that the disk surface consisted of parallel grooves/ridges with $R_a = 0.599 \mu\text{m}$. Compared with the worn pin surfaces, the disk surfaces after sliding wear were much smoother at both temperatures.

G. Wear-Induced Subsurface Microstructural Evolution

To understand this wear behavior and reveal its wear mechanism, wear-induced subsurface microstructures were characterized by cross-sectional FIB/TEM. SE images of FIB-milled ND–SD cross-sections yielded good contrast over large fields of view. TEM/

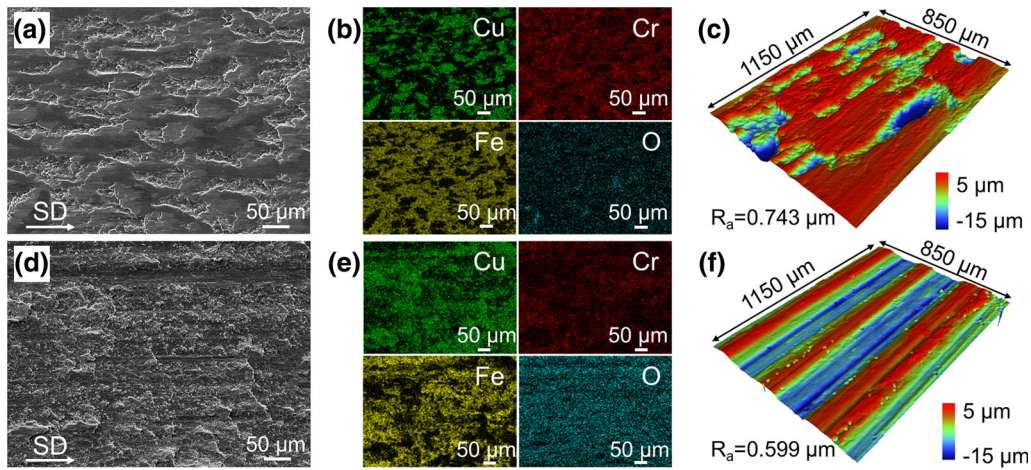


Fig. 10—Characterization of the wear track. (a) through (c) show an SEM image, EDX elemental maps, and 3D surface profile of the wear track measured at room temperature, respectively; (d) through (f) show the analogous data measured at 300 °C.

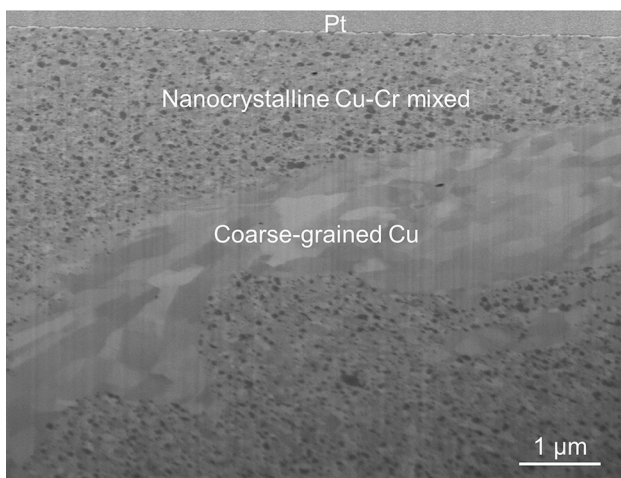


Fig. 11—SE image of an FIB-milled ND-SD cross-section of Cu-6 wt pct Cr alloy after sliding against SS 440C at room temperature.

STEM-based analytical techniques were then used to extract more detailed chemistry, crystallography, and microstructure information.

Figure 11 shows an ND-SD cross-sectional SE image of the subsurface microstructure of the alloy after sliding wear at RT. No appreciable plastic deformation was found in the nanostructured Cu-Cr mixed zone, but significant shear deformation occurred in the coarse-grained Cu zone. Figures 12(a, b) present ND-SD cross-sectional HAADF-STEM and corresponding bright-field TEM images. EDX analyses (Figure 12(c)) showed that three phases were present, which were similar to those found in the Cu-6 wt pct Cr alloy before wear testing (Figures 3(a, b)). The trace amount of Fe detected in the EDX spectra was probably from the counterface disk. Cross-sectional HAADF-STEM and bright-field TEM images and the SAED patterns

obtained at different depths (Figures 12(d, e)) revealed that no apparent deformed layer was present below the sliding surface. The SAED patterns obtained at two distinct depths from the sliding surface showed almost no difference, suggesting that no glaze layer formed at RT.

On wear exposure at 300 °C, the worn pin surface contained two distinct characteristic regions: oxygen-deficient grooves and oxygen-rich ridges, as marked in Figure 13(a). The corresponding distribution of oxygen is shown in Figure 13(b). The cross-sectional subsurface microstructures were separately characterized for both regions. Figure 13(c) presents an ND-SD cross-sectional SE image obtained from the grooves (area A). No glaze layer was found in this region. Detailed characterization by TEM and HAADF-STEM with EDX chemical analysis is presented in Figure 14. Below the sliding surface, an SPD region with elongated Cu grains and uniformly dispersed Cr-rich and Cr oxide nanoparticles was observed, extending to a depth of $\sim 1 \mu\text{m}$ (Figure 14(a)). Such wear-induced deformation is similar to that of Cu-W alloy,^[51] but not as obvious as that found in Cu-Ag^[54] and Nb-Ag^[37] alloys, because the uniformly dispersed Cr-rich/Cr oxide nanoparticles would impede dislocation motion. HAADF-STEM and EDX elemental maps (Figures 14(b, c)) showed that the SPD region consisted of Cu, Cr-rich nano-precipitates, and a small amount of Cr oxides.

A glaze layer with a thickness of $\sim 1.1 \mu\text{m}$ was formed on oxygen-rich ridges, as shown in Figure 13(d). Below the glaze layer, the deformed pin matrix had a microstructure similar to that in the oxygen-deficient grooves, while the SPD region extended to a depth of $\sim 3.5 \mu\text{m}$. Coarse-grained Cu was also found at $\sim 3 \mu\text{m}$ away from the sliding surface. Several twin boundaries were observed in the coarse-grained Cu zone. Bright-

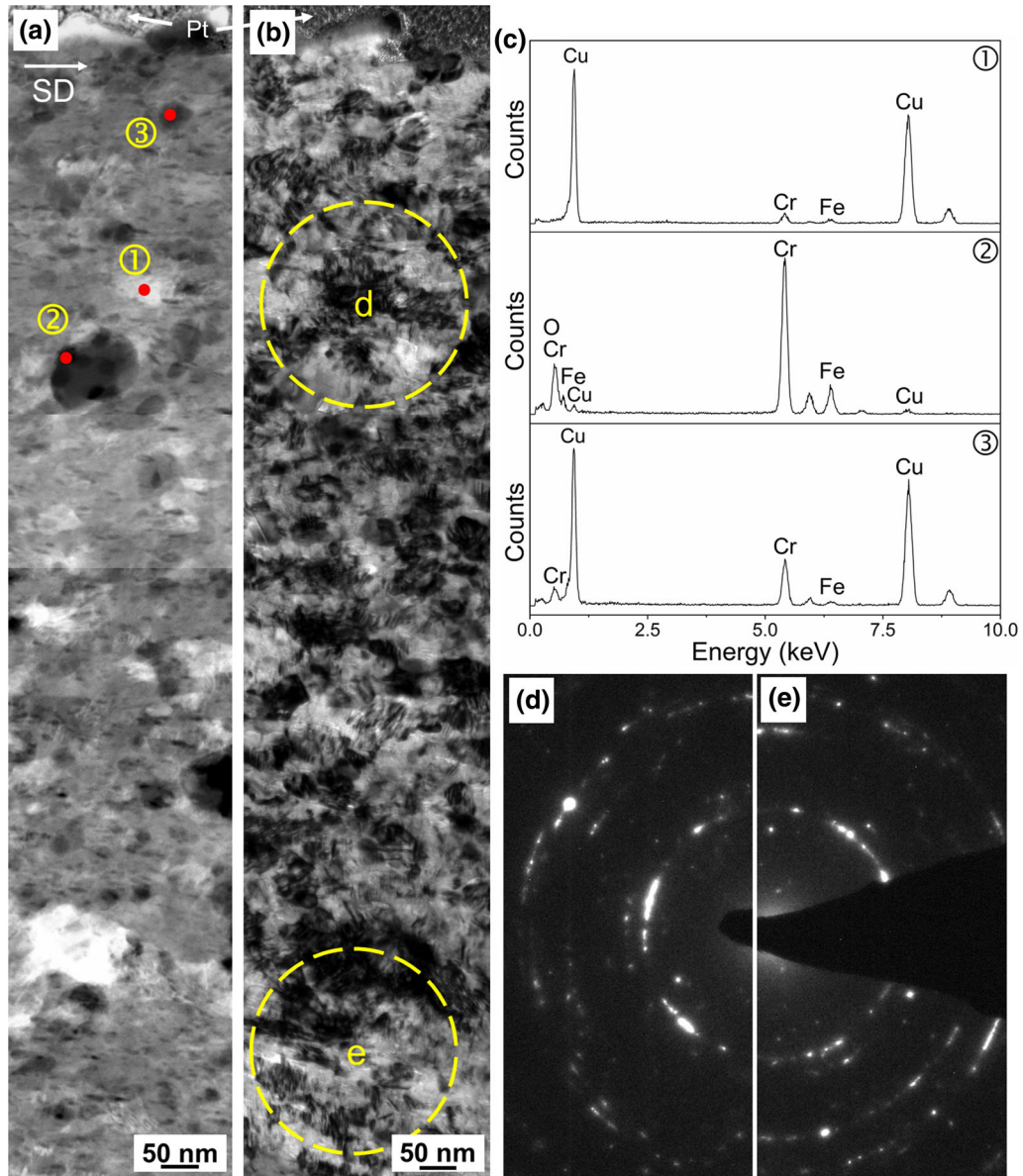


Fig. 12—ND-SD cross-sectional microstructure of Cu-6 wt pct Cr alloy after sliding wear against SS 440C at room temperature. (a) and (b) show HAADF-STEM and corresponding bright-field TEM images, respectively; (c) EDX spectra obtained from the three contrasts in (a); (d) and (e) are SAED patterns obtained from the regions marked in (b).

field TEM (Figure 15(a)) and corresponding SAED patterns (Figure 15(b-d)) revealed that the glaze layer consisted of equiaxed nanocrystalline (several nanometers) Cu, Cu oxides, and Cr oxides. The Cu oxides were mainly in the form of Cu_2O (JCPDS No. 99-0041, space

group Pn-3m) and the Cr oxides were Cr_5O_{12} (JCPDS No. 73-1787, Pbcn), CrO_2 (JCPDS No. 89-3079, $\text{P4}_2/\text{mm}$), and Cr_3O_4 (JCPDS No. 12-0559, $\text{I4}_1/\text{amd}$). These species were further confirmed by HRTEM analyses (Figure 16).

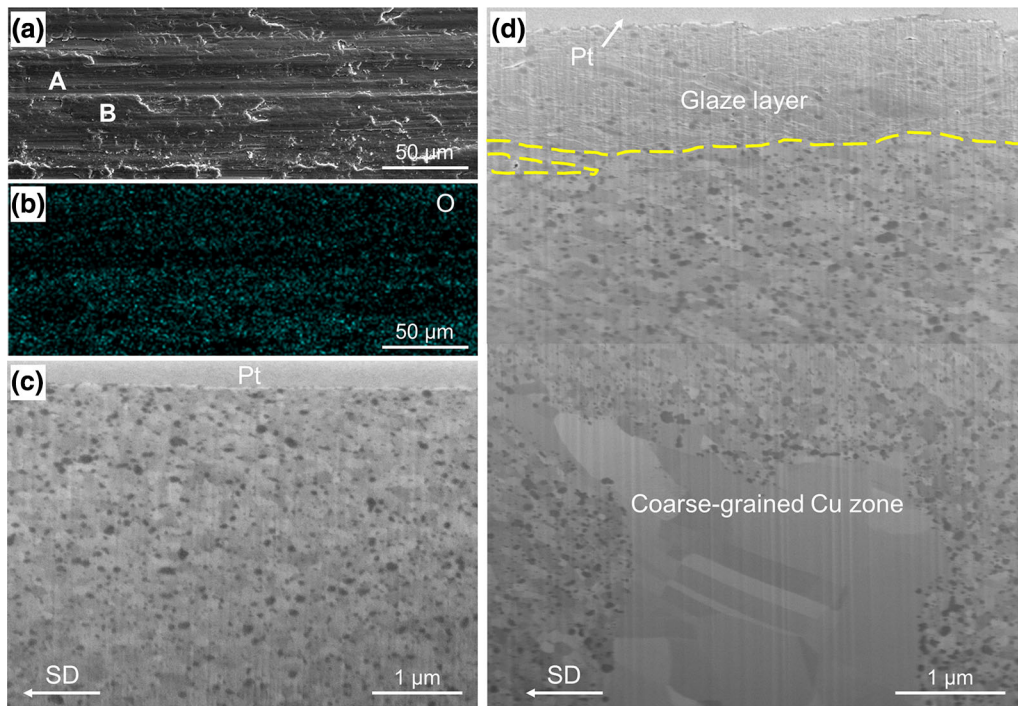


Fig. 13—(a) and (b) show an SEM image and corresponding EDX elemental map of oxygen of a selected representative area from the worn pin surface upon wear exposure at 300 °C, respectively; (c) and (d) show SE images of the FIB-milled ND–SD cross-sections corresponding to areas A and B in (a), respectively.

IV. DISCUSSION

This work focused on the wear mechanism and evolution of wear-induced subsurface microstructures in Cu-6 wt pct Cr alloy with a heterogeneous microstructure and its correlation with wear performance at RT and 300 °C. The results clearly indicated that both the coefficient of friction and wear rate were higher at 300 °C than those at RT. The primary wear mode switched from adhesion at RT to abrasion and oxidation at 300 °C.

At RT, a very limited amount of oxides formed during wear, as confirmed by composition analyses on both the contact surfaces and in the wear debris. A minor amount of chromium oxides was generated during fabrication of the alloy. The metal-to-metal contact and plastic deformation of the fabricated Cu-6 wt pct alloy yielded wear debris in the form of large flakes and material transfer from the pin surface to the counterface disk. The coefficient of friction of 0.62 ± 0.03 is typical for dry sliding of metallic materials and

the adhesive wear mode is common for Cu-based alloys upon sliding against metallic mating materials.^[4,36,51,55–59]

On wear exposure at 300 °C, the oxidation reaction would significantly influence the wear behavior, as observed in other alloys at elevated temperatures.^[37–41,60] The kinetics of metallic surface oxidation has a controlling effect on oxidative wear, while the oxidation rate of the metals is dependent on temperature. The generated wear debris that remained on the worn surface was oxidized and compacted into a glaze layer.^[61] With progression of sliding wear, the formed glaze layer breaks down to form debris and the debris particles sinter to consolidate the layer. These two processes compete during sliding.^[41] A stable thick glaze layer can protect the substrate from severe wear and thereby improve the wear resistance.^[42,62] Kinetically, increasing temperature could increase the oxidation rate of metals in the debris and accelerate sintering and consolidation of the glaze layer.^[41] If the temperature is not sufficiently high, however, the particles would not be

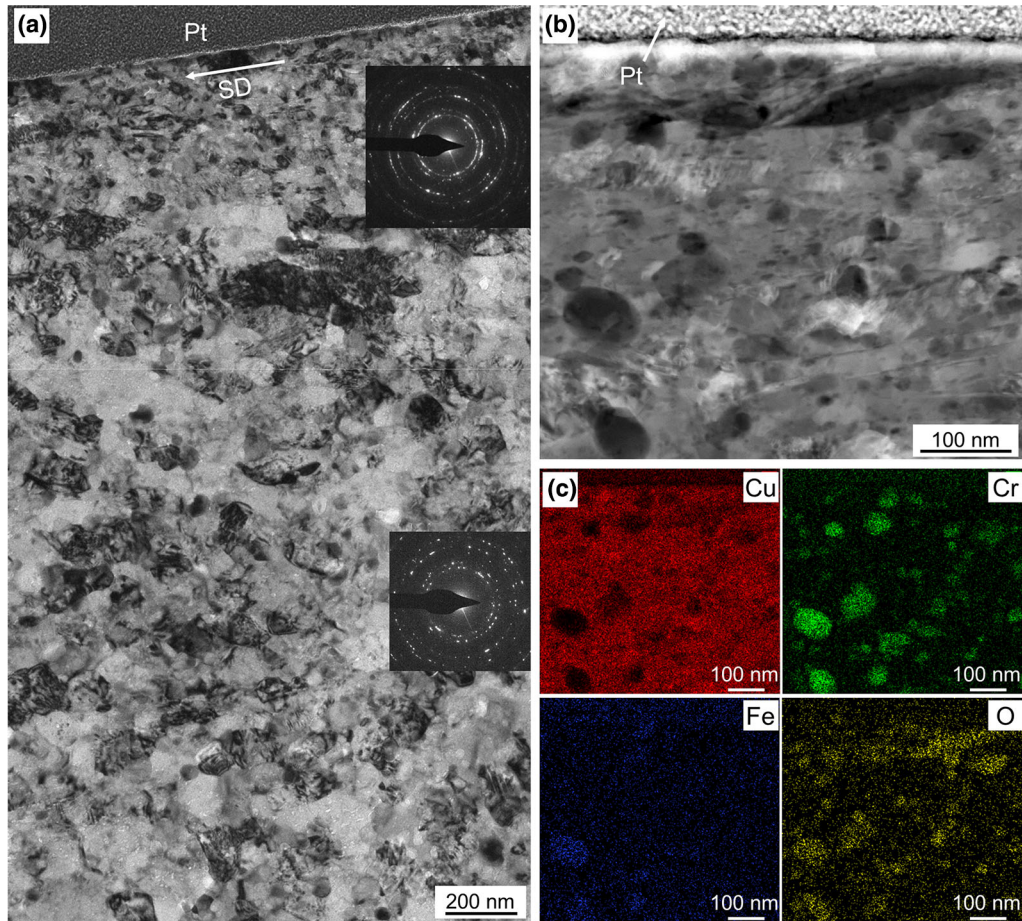


Fig. 14—TEM/STEM characterization of ND–SD cross-sectional microstructure of Cu-6 wt pct Cr alloy after sliding wear against SS 440C at 300 °C in the grooves without glaze layer. (a) Bright-field TEM image; (b) and (c) show the HAADF-STEM image and the EDX elemental maps, respectively.

well sintered to establish a stable protective glaze layer and the generated hard oxides may plow the surface, leading to severe abrasion-assisted wear, generation of grooves on the worn surface of the pin, and a high wear rate. In this work, the moderate temperature of 300 °C was obviously unable to provide sufficient oxidation or adequate sintering rates of debris particles on the worn pin surface, as confirmed by the ND–SD cross-sectional microstructure after wear (Figure 15), which showed that non-oxidized Cu still existed in the glaze layer. The wear debris contained a large amount of Cu and Cr oxides, including CuO, Cu₂O, and Cr₅O₁₂. Such oxides have much higher hardness; for example, Mohs hardnesses of CuO and Cu₂O are 3.4 and 4, respectively.^[63] These hard oxide particles could plow the pin surface, causing abrasive wear, generation of grooves on the worn surface of the pin (as observed in Figure 9(d)), and

an increase in wear rate at 300 °C. High temperature may also cause thermal softening and grain growth in the alloy. To verify this, the hardness and compressive test of the Cu-6 wt pct Cr alloy were performed at 300 °C and the Cu grain and Cr-rich precipitate sizes in the base alloy were statistically measured in a region far away from the sliding surface after wear at 300 °C for 10⁴ s (sliding distance of 1000 m and a sliding velocity of 0.1 m/s). The hardness decreased by ~ 25 pct, from 246 HV at RT to 185 HV at 300 °C. The average Cu grain and Cr-rich precipitate sizes increased to 95 and 41 nm, respectively, as shown in Figure 17. Such thermal softening and grain growth is also expected to contribute to the high wear rate at 300 °C.

The wear-induced microstructures at RT and 300 °C differed considerably. At RT, no obvious plastic deformation below the sliding surface was observed, which

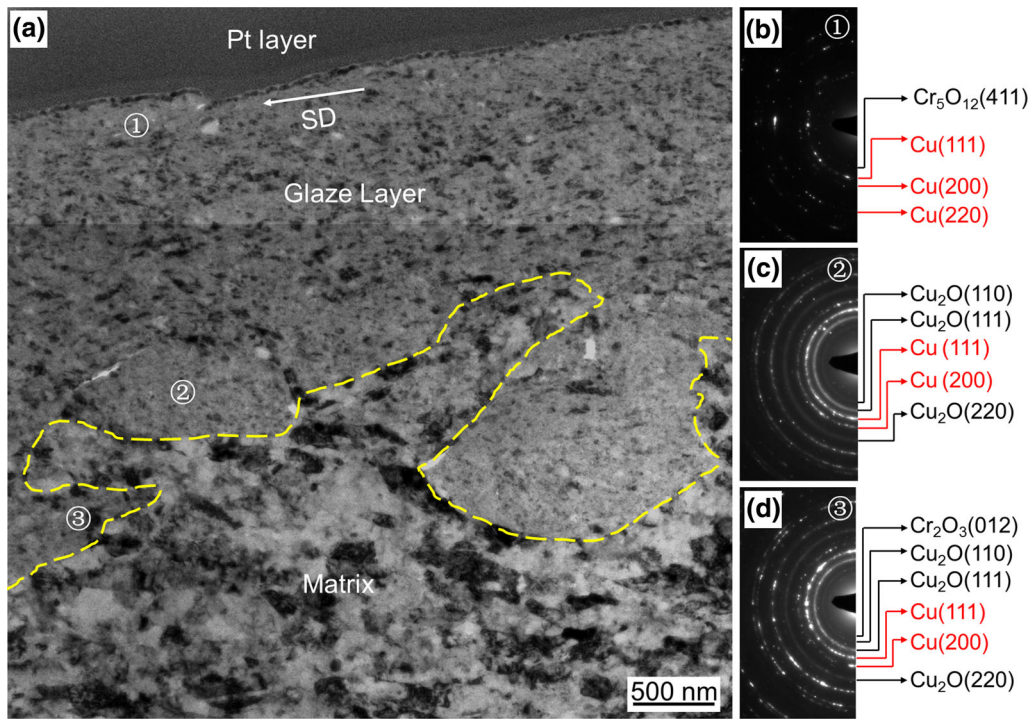


Fig. 15—TEM characterization of ND-SD cross-sectional microstructure of Cu-6 wt pct Cr alloy after sliding wear at 300 °C in the ridges with glaze layer. (a) Bright-field TEM image, (b) through (d) show SAED patterns of the glaze layer obtained at different depths from the sliding surface marked in (a).

was attributed to hindering of plastic deformation of the nanocrystalline Cu-Cr matrix in the spark plasma-sintered Cu-6 wt pct Cr alloy by nanoscale hard Cr-rich and/or Cr oxide precipitates, similar to that of nanocrystalline Cu-10 at. pct W alloy.^[51] When the temperature was raised to 300 °C, the wear-induced microstructure contained an SPD region with elongated Cu grains. Elevated temperature will facilitate by-passing of precipitates by grain boundary dislocations through glide/climb mechanisms. In addition, grain rotation probably also served as an important deformation mechanism at elevated temperature: under these conditions, dislocations may move continuously across grain boundaries through grain rotations.

V. CONCLUSIONS

A bulk Cu-6 wt pct Cr alloy was fabricated by a combination of HEBM and SPS and its wear behavior was systematically investigated at RT and 300 °C. The following major conclusions were drawn:

1. The spark plasma-sintered Cu-6 wt pct Cr alloy showed a heterogeneous microstructure, consisting of coarse-grained Cu distributed into a nanocrystalline Cu-Cr matrix. The coarse-grained Cu had an average size of 1.5 μm , while the nanocrystalline Cu-Cr matrix had Cu grains of 77 nm in size and uniformly dispersed Cr-rich precipitates of 18 nm.
2. The heterogeneous microstructure enabled high strength and plasticity with an ultimate compressive

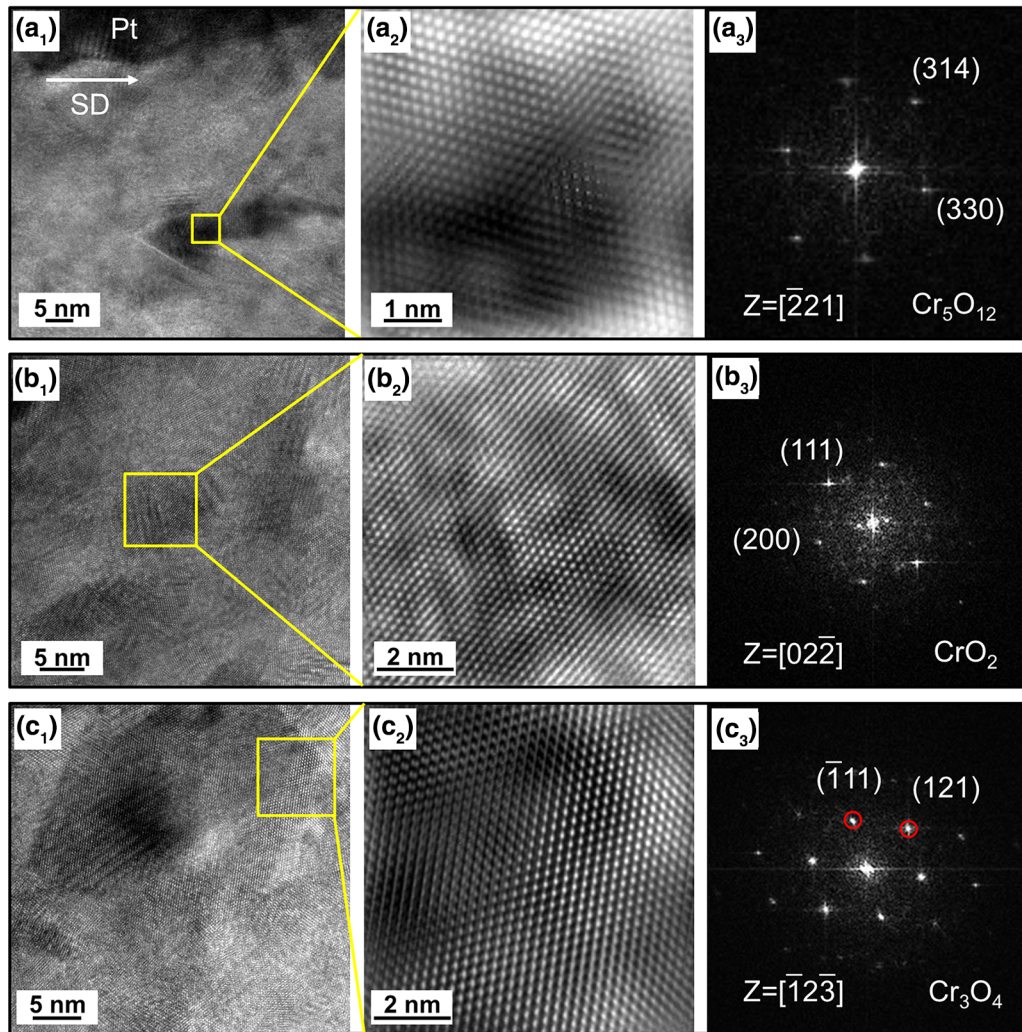


Fig. 16—HRTEM characterization of different chromium oxides present in the glaze layer. (a_1) through (a_3) show an HRTEM image, higher magnification HRTEM image of the selected area, and corresponding inverse Fourier transform (IFFT) image of Cr_5O_{12} , respectively; (b_1) through (b_3) and (c_1) through (c_3) show the analogous data for CrO_2 and Cr_3O_4 , respectively.

- strength of 1020 MPa and strain-to-failure of 26.0 pct, and hardness of $246 (\pm 12)$ HV at RT.
- On increasing the temperature from RT to 300 °C, the strength was significantly reduced and both the coefficient of friction and wear rate increased. The primary wear mode switched from adhesion at RT to abrasion and oxidation at 300 °C.
 - At RT, no glaze layer was formed. The coarse-grained Cu showed pronounced plastic deformation, but the nanocrystalline Cu-Cr matrix showed no significant difference from its initial state, owing to hindering of plastic deformation by the nanoscale Cr-rich or Cr oxide precipitates.
 - At 300 °C, a discontinuous glaze layer consisting of equiaxed nanocrystalline Cu, Cu oxides, and Cr oxides was formed. An SPD region with elongated Cu grains and uniformly dispersed Cr-rich and Cr oxide nanoparticles was observed. The generated hard oxides would plow the surface and lead to severe abrasion-assisted wear.

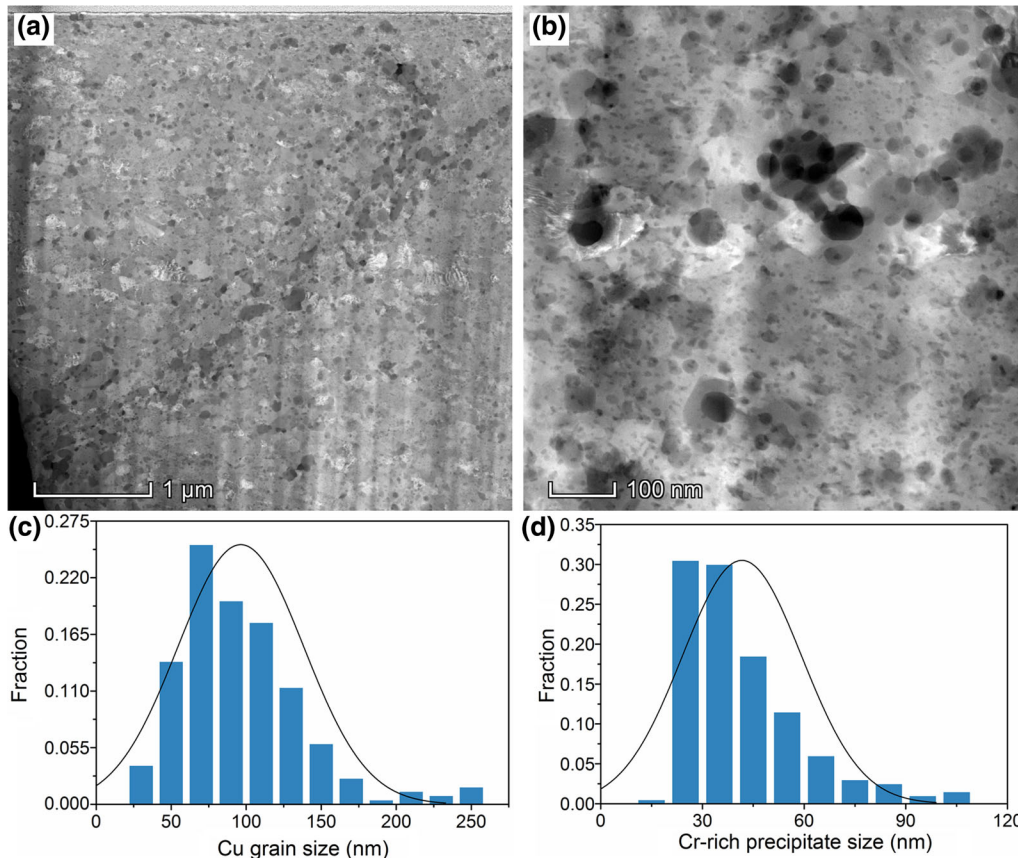


Fig. 17—Cu grain and Cr-rich precipitate size distributions of nanocrystalline Cu-Cr matrix in Cu-6 wt pct Cr alloy after wear at 300 °C. (a) and (b) show HAADF-STEM images at different magnifications; (c) and (d) show Cu grain size and Cr-rich precipitate size distributions, respectively.

ACKNOWLEDGMENTS

This work was financially supported by the National Natural Science Foundation of China (Grant No. 51874204), and the Fundamental Research Program of Shenzhen (Grant Nos. JCYJ20170412153039309 and JCYJ20170307110418960).

REFERENCES

- G. Purcek, H. Yanar, O. Saray, I. Karaman, and H.J. Maier: *Wear*, 2014, vol. 311, pp. 149–58.
- I.S. Batra, G.K. Dey, U.D. Kulkarni, and S. Banerjee: *J. Nucl. Mater.*, 2001, vol. 299, pp. 91–100.
- N. Takata, Y. Ohtake, K. Kita, K. Kitagawa, and N. Tsuji: *Scripta Mater.*, 2009, vol. 60, pp. 590–93.
- H. Nagasawa and K. Kato: *Wear*, 1998, vol. 216, pp. 179–83.
- Q. Fang, Z.X. Kang, Y.W. Gan, and Y. Long: *Mater. Des.*, 2015, vol. 88, pp. 8–15.
- G. Purcek, H. Yanar, D.V. Shangina, M. Demirtas, N.R. Bocharov, and S.V. Dobatkin: *J. Alloy. Compd.*, 2018, vol. 742, pp. 325–33.
- R.K. Gautam, S. Ray, S.C. Sharma, S.C. Jain, and R. Tyagi: *Wear*, 2011, vol. 271, pp. 658–64.
- A.K. Shukla, R.S. Kumar, S.V.S.N. Murty, and K. Mondal: *Mater. Sci. Eng. A*, 2013, vol. 577, pp. 36–42.
- J.P. Tu, W.X. Qi, Y.Z. Yang, F. Liu, J.T. Zhang, G.Y. Gan, N.Y. Wang, X.B. Zhang, and M.S. Liu: *Wear*, 2001, vol. 249, pp. 1021–27.
- Y. Zhang, A.A. Volinsky, H.T. Tran, Z. Chai, P. Liu, B.H. Tian, and Y. Liu: *Mater. Sci. Eng. A*, 2016, vol. 650, pp. 248–53.
- N.Y. Tang, D.M.R. Taplin, and G.L. Dunlop: *Mater. Sci. Technol.*, 1985, vol. 1, pp. 270–75.
- T. Fujii, H. Nakazawa, M. Kato, and U. Dahmen: *Acta Mater.*, 2000, vol. 48, pp. 1033–45.
- F.X. Huang, J.S. Ma, H.L. Ning, Z.T. Geng, C. Lu, S.M. Guo, X.T. Yu, T. Wang, H. Li, and H.F. Lou: *Scripta Mater.*, 2003, vol. 48, pp. 97–102.
- P. Liu, J. Su, Q. Dong, and H. Li: *J. Mater. Sci. Technol.*, 2005, vol. 21, pp. 475–78.
- H.T. Zhou, J.W. Zhong, X. Zhou, Z.K. Zhao, and Q.B. Li: *Mater. Sci. Eng. A*, 2008, vol. 498, pp. 225–30.
- J.H. Su, Q.M. Dong, P. Liu, H.J. Li, and B.X. Kang: *Mater. Sci. Eng. A*, 2005, vol. 392, pp. 422–26.
- Z.L. Zhang, J.M. Guo, G. Dehm, and R. Pippan: *Acta Mater.*, 2017, vol. 138, pp. 42–51.
- J.M. Guo, J.L. Rosalie, R. Pippan, and Z.L. Zhang: *Scripta Mater.*, 2017, vol. 133, pp. 41–44.
- A. Bachmaier, G.B. Rathmayr, M. Bartosik, D. Apel, Z. Zhang, and R. Pippan: *Acta Mater.*, 2014, vol. 69, pp. 301–13.
- A. Vinogradov, V. Patlan, Y. Suzuki, K. Kitagawa, and V.I. Kopylov: *Acta Mater.*, 2002, vol. 50, pp. 1639–51.
- R. Mishnev, I. Shakhova, A. Belyakov, and R. Kaibyshev: *Mater. Sci. Eng. A*, 2015, vol. 629, pp. 29–40.
- K.X. Wei, W. Wei, F. Wang, Q.B. Du, I.V. Alexandrov, and J. Hu: *Mater. Sci. Eng. A*, 2011, vol. 528, pp. 1478–84.
- K.V. León, M.A. Muñoz-Morris, and D.G. Morris: *Mater. Sci. Eng. A*, 2012, vol. 536, pp. 181–89.
- M. Kulczyk, B. Zysk, M. Lewandowska, and K.J. Kurzydłowski: *Phys. Status Solidi A*, 2010, vol. 207, pp. 1136–38.
- C. Aguilar, V.D.P. Martinez, J.M. Palacios, S. Ordoñez, and O. Pavez: *Scripta Mater.*, 2007, vol. 57, pp. 213–16.
- Q. Fang and Z.X. Kang: *Powder Technol.*, 2015, vol. 270, pp. 104–11.

27. S.H. Dong, C.L. Zhang, L.Y. Zhang, J. Cai, P. Lv, Y.X. Jin, and Q.F. Guan: *J. Alloy. Compd.*, 2018, vol. 755, pp. 251–56.
28. I. Lahiri and S. Bhargava: *Powder Technol.*, 2009, vol. 189, pp. 433–38.
29. G. Lee, E.A. Olefsky, C. Manière, A. Maximenko, O. Izhvanov, C. Back, and J. McKittrick: *Acta Mater.*, 2018, vol. 144, pp. 524–33.
30. K.B. Gerasimov, S.V. Mytnichenko, S.V. Pavlov, V.A. Chernov, and S.G. Nikitenko: *J. Alloy. Compd.*, 1997, vol. 252, pp. 179–83.
31. S. AsadiKouhanjani, A. ZareBidaki, and A. Akbari: *J. Alloy. Compd.*, 2009, vol. 486, pp. 319–24.
32. S. AsadiKouhanjani, A. ZareBidaki, M. Abedini, and N. Parvin: *J. Alloy. Compd.*, 2009, vol. 480, pp. 505–09.
33. W.X. Qi, J.P. Tu, F. Liu, Y.Z. Yang, N.Y. Wang, H.M. Lu, X.B. Zhang, S.Y. Guo, and M.S. Liu: *Mater. Sci. Eng. A*, 2003, vol. 343, pp. 89–96.
34. J.F. Curry, T.F. Babuska, T.A. Furnish, P. Lu, D.P. Adams, A.B. Kustas, B.L. Nation, M.T. Dugger, M. Chandross, B.G. Clark, B.L. Boyce, C.A. Schuh, and N. Argibay: *Adv. Mater.*, 2018, vol. 30, p. 1870242.
35. X. Chen, Z. Han, X.Y. Li, and K. Lu: *Sci. Adv.*, 2016, vol. 2, p. e1601942.
36. D.A. Rigney: *Wear*, 2000, vol. 245, pp. 1–9.
37. K.J. Chu, J. Zhou, and F.Z. Ren: *Wear*, 2018, vols. 414–415, pp. 251–61.
38. J.R. Jiang, F.H. Stott, and M.M. Stack: *Wear*, 1995, vols. 181–183, pp. 20–31.
39. F.H. Stott, D.S. Lin, G.C. Wood, and C.W. Stevenson: *Wear*, 1976, vol. 36, pp. 147–74.
40. J. Jiang, F.H. Stott, and M.M. Stack: *Wear*, 1997, vol. 203, pp. 615–25.
41. A. Pauschitz, M. Roy, and F. Franek: *Tribol. Int.*, 2008, vol. 41, pp. 584–602.
42. C. Rynio, H. Hattendorf, J. Klöwer, and G. Eggeler: *Wear*, 2014, vol. 315, pp. 1–10.
43. E. Ma: *Prog. Mater. Sci.*, 2005, vol. 50, pp. 413–509.
44. C. Suryanarayana: *Prog. Mater. Sci.*, 2001, vol. 46, pp. 1–184.
45. A.P. Zhilyaev and T.G. Langdon: *Prog. Mater. Sci.*, 2008, vol. 53, pp. 893–979.
46. A. Takeuchi and A. Inoue: *Mater. Trans.*, 2005, vol. 46, pp. 2817–29.
47. P. Hvizdoš, M. Besterci, and P. Kulu: *High Temp. Mater. Process.*, 2011, vol. 30, pp. 573–77.
48. S. Mula, P. Sahani, S.K. Pratihar, S. Mal, and C.C. Koch: *Mater. Sci. Eng. A*, 2011, vol. 528, pp. 4348–56.
49. P. Sahani, S. Mula, P.K. Roy, P.C. Kang, and C.C. Koch: *Mater. Sci. Eng. A*, 2011, vol. 528, pp. 7781–89.
50. S. Bera, S.G. Chowdhury, W. Lojkowsky, and I. Manna: *Mater. Sci. Eng. A*, 2012, vol. 558, pp. 298–308.
51. F.Z. Ren, W.W. Zhu, K.J. Chu, and C.C. Zhao: *J. Alloy. Compd.*, 2016, vol. 676, pp. 164–72.
52. G. Straffelini, L. Maines, M. Pellizzari, and P. Scardi: *Wear*, 2005, vol. 259, pp. 506–11.
53. J. Don, T.C. Sun, and D.A. Rigney: *Wear*, 1983, vol. 91, pp. 191–99.
54. F. Ren, S.N. Arshad, P. Bellon, R.S. Averback, M. Pouryazdan, and H. Hahn: *Acta Mater.*, 2014, vol. 72, pp. 148–58.
55. S. Kang: *Wear*, 1993, vols. 162–164, pp. 1123–28.
56. A. Emge, S. Karthikeyan, and D.A. Rigney: *Wear*, 2009, vol. 267, pp. 562–67.
57. W. Cai and P. Bellon: *Acta Mater.*, 2012, vol. 60, pp. 6673–84.
58. J.B. Singh, W. Cai, and P. Bellon: *Wear*, 2007, vol. 263, pp. 830–41.
59. W. Cai and P. Bellon: *Wear*, 2013, vol. 303, pp. 602–10.
60. I.A. Inman, S.R. Rose, and P.K. Datta: *Wear*, 2006, vol. 265, pp. 1592–1605.
61. G.W. Stachowiak and A.W. Batchelor: in *Engineering Tribology (Third Edition)*, ed. G.W. Stachowiak and A.W. Batchelor, eds., Butterworth-Heinemann, Burlington, 2006, pp. 573–93.
62. F.F.H. Stott: *Tribol. Int.*, 1998, vol. 31, pp. 61–71.
63. M.B. Peterson, S.F. Murray, and J.J. Florek: *ASLE Trans.*, 1959, vol. 2, pp. 225–34.

Publisher's Note Springer Nature remains neutral with regard to jurisdictional claims in published maps and institutional affiliations.